Journal of the European Ceramic Society 23 (2003) 961–976

www.elsevier.com/locate/jeurceramsoc

Low pressure plasma-sprayed Al_2O_3 and Al_2O_3/SiC nanocomposite coatings from different feedstock powders

S. Jiansirisomboon[a,*], K.J.D. MacKenzie[b], S.G. Roberts[a], P.S. Grant[a]

[a]*Department of Materials, University of Oxford, Parks Road, Oxford OX1 3PH, UK*
[b]*New Zealand Institute for Industrial Research and Development, PO Box 31-310, Lower Hutt, New Zealand*

Received 4 July 2001; accepted 16 June 2002

Abstract

This paper describes a preliminary investigation of a nanocomposite ceramic coating system, based on Al_2O_3/SiC. Feedstock Al_2O_3/SiC nanocomposite powder has been manufactured using sol-gel and conventional freeze-drying processing techniques and then low pressure plasma sprayed onto stainless steel substrates using a CoNiCrAlY bond coat. Coatings of a commercial Al_2O_3 powder have also been manufactured as a reference for phase transformations and microstructure. The different powder morphology and size distribution resulting from the different processing techniques and their effect on coating microstructure has been investigated. Phase analysis of the feedstock powders and of the as-sprayed coatings by X-ray diffractometry (XRD) and nuclear magnetic resonance (NMR) showed that the nano-scale SiC particles were retained in the composite coatings and that equilibrium α-Al_2O_3 transformed to metastable γ- and δ-Al_2O_3 phases during plasma spraying. Other minority phases in the sol-gel Al_2O_3/SiC nanocomposite powder such as silica and aluminosilicate were removed by the plasma-spraying process. Microstructure characterisation by scanning electron microscopy (SEM) of the as-sprayed surface, polished cross-section, and fracture surface of the coatings showed evidence of partially molten and unmolten particles incorporated into the predominantly lamella microstructure of the coating. The extent of feedstock particle melting and consequently the character of the coating microstructure were different in each coating because of the effects of particle morphology and particle size distribution on particle melting in the plasma.

Keywords: Al_2O_3; Al_2O_3/SiC; Coatings; Nanocomposites; Plasma spraying

1. Introduction

Plasma spray ceramic coatings are widely used to provide surface resistance to corrosion, heat and wear for alloy and metal components, and consequently to extend service life. Plasma spraying is a complex process, which combines the injection of solid particles into a plasma jet created by either a d.c. arc or an r.f. field, the melting of these particles in the high temperature region in the plasma "flame", and the consolidation of the sprayed molten droplets on a substrate to form a coherent coating. In most cases, the microstructure of the as-sprayed coating consists of a complex inter-locking network of individual droplet splats or lamellae. The quality of plasma-sprayed coatings in terms of adhesion, porosity and roughness is controlled by the trajectory and thermal history of the plasma particles in the plasma flame, which in turn is controlled by manipulation of, for instance, the plasma Ar–H_2 flow rate, particle flow rate, chamber pressure and spray distance.

Plasma spraying may lead to rapid solidification phenomena in the droplets following deposition at a surface, resulting in metastable crystalline phases and amorphous structures. Spraying may also be accompanied by a change of chemical composition, for instance by preferential evaporation of some particle feedstock elements, and the spraying atmosphere may also induce particle oxidation or reduction. Consequently, major factors affecting the final phase composition of plasma sprayed coatings are: (a) phase, chemical composition and morphology of the feedstock powder and (b) spraying conditions, particularly spraying atmosphere and spraying parameters which Influence rapid solidification and rapid cooling processes.[1]

* Corresponding author at current address: Department of Physics, Faculty of Science, Chiang Mai University, Chiang Mai, 50200, Thailand. Tel.: +66-53-943376; fax: +66-53-357512.
E-mail address: sukanda@chiangmai.ac.th (S. Jiansirisomboon).

0955-2219/03/$ - see front matter
PII: S0955-2219(02)00207-8

Plasma-sprayed Al_2O_3 and its composites such as Al_2O_3–TiO_2, Al_2O_3–Cr_2O_3 are used widely in wear resistant coating applications.[2,3] It has been known for some time that sprayed Al_2O_3 coatings may consist not only of the expected stable α-form, which is the most desirable phase because of its relatively high corrosion resistance, chemical resistance and hardness, but also the metastable γ-, δ-, and θ-phase forms of Al_2O_3.[4–8]

In this study, Al_2O_3 is used a base for a nanocomposite coating system prepared from Al_2O_3/SiC nanocomposite powders. The particular interest in nanocomposite powders has been driven by reports that the addition of nano-size SiC particles of 100–200 nm into an Al_2O_3 matrix can significantly improve the mechanical properties over those of monolithic Al_2O_3.[9–11] Recently, the polishing behaviour and surface quality after grinding and polishing of a Al_2O_3/SiC nanocomposite has been reported to be superior to that of monolithic Al_2O_3.[12] An increase in erosive wear resistance by a factor of 2–3 of Al_2O_3/SiC nanocomposite bulk material over the monolithic Al_2O_3 of equivalent grain size has also been suggested.[11,13–16]

This paper describes the manufacture of Al_2O_3/SiC nanocomposite coatings using in-house produced sol-gel and freeze-dried powder, followed by low pressure plasma spraying (LPPS). The powders and coatings are investigated by a combination of X-ray diffraction (XRD), nuclear magnetic resonance (NMR), scanning electron microscopy (SEM), surface roughness measurement and quantitative image analysis. Microstructural features are explained in terms of the feedstock powder particles and the thermal history of the particles during manufacture.

2. Experimental procedure

2.1. Materials

Powders used were monolithic commercial alumina (Amdry6060, Sulzer Metco, UK) and alumina/silicon carbide (Al_2O_3/SiC) nanocomposite powders. In each case, the Al_2O_3 was composed primarily of α-Al_2O_3. The nanocomposite powder was prepared in-house using sol-gel processing and conventional freeze-drying.

2.2. Sol-gel powders

As-received SiC powder (Lonza-UF45, Germany) of diameter ~20–200 nm was ultrasonically dispersed in distilled water (500 ml) for at least 1 h and then vigorously stirred using a magnetic stirrer. 0.5 M of $Al(NO_3)_3{\cdot}9H_2O$ (100.5 g/500 ml distilled water) and NH_4OH solutions were peptised into the SiC solution at controlled pH ≈9. After precipitation of boehmite (AlOOH) which was the starting material for Al_2O_3 from this solution was complete, the mixture was filtered and subsequently washed with distilled water. The washed mixture was again filtered and then oven-dried at 85C overnight. The as-reacted precipitate was calcined at 1200 °C for 2 h, ball-milled, and sieved down into two different particle diameters of <45 μm (SG45) and 45–63 μm (SG6345). Fig. 1(a) shows the processing flow chart of the sol-gel Al_2O_3/SiC powder.

2.3. Freeze-dried powders

Freeze-dried Al_2O_3/SiC nanocomposite powders (10 and 20 vol.% SiC) were fabricated from α-Al_2O_3 powder (AES11C, Sumitomo, Japan) and α-SiC powder (Lonza-UF45, Germany) with mean quoted particle diameters of 400 and 200 nm, respectively. The SiC powder was ultrasonically dispersed in distilled water for 20 min. The SiC solution, Al_2O_3 powder, and 10 drops of dispersing agent (Dispex A40, Allied Colloids) were mixed and attrition-milled for 2 h at a speed of 500 rpm using zirconia milling media. Subsequently, the water-based slurry was frozen in an ethanol bath for 1 h and immediately vacuum-dried for at least 24 h. The dried powder was then sieved to diameter <45 μm (FD45). Freeze-dried monolithic Al_2O_3 was prepared by following the above sequences without adding the SiC particles. Fig. 1(b) shows the processing flow chart of freeze-dried Al_2O_3/SiC powders.

The particle size distribution of each powder was carried out by laser diffraction on Mastersizer 2000 system (Malvern Instruments Ltd., UK). Powder morphologies were observed using a Hitachi S520 scanning electron microscope.

2.4. Low pressure plasma spraying

Powders were sprayed onto stainless steel substrates (22 mm diameter, 5 mm thick), which were degreased and blasted with alumina grit (particle size 120–220 μm) in order to provide sufficient surface topography to promote mechanical adhesion of the sprayed coatings. In each case, a bond coat was used to further enhance the adhesion of the Al_2O_3 based coatings. The CoNiCrAlY bond coat had composition Co-211-3: Co, 32% Ni, 21% Cr, 8% Al, 0.5% Y_2O_3 with a particle size of 50–130 μm (Praxair Surface Technologies).

A Plasma-Technik A2000 VPS/LPPS system (Sulzer Metco AG, Wohlen, Switzerland) was used to manufacture the bond and Al_2O_3-based coatings. In preliminary experiments, it was found that a water-cooled substrate holder system, which maintained a low substrate temperature during and after spraying, was needed to inhibit the spalling of some of the Al_2O_3 based sprayed coatings because of coefficient of thermal expansion mismatch. For nanocomposite coatings, an additional thin layer of Al_2O_3 was also sprayed onto the CoNiCrAlY

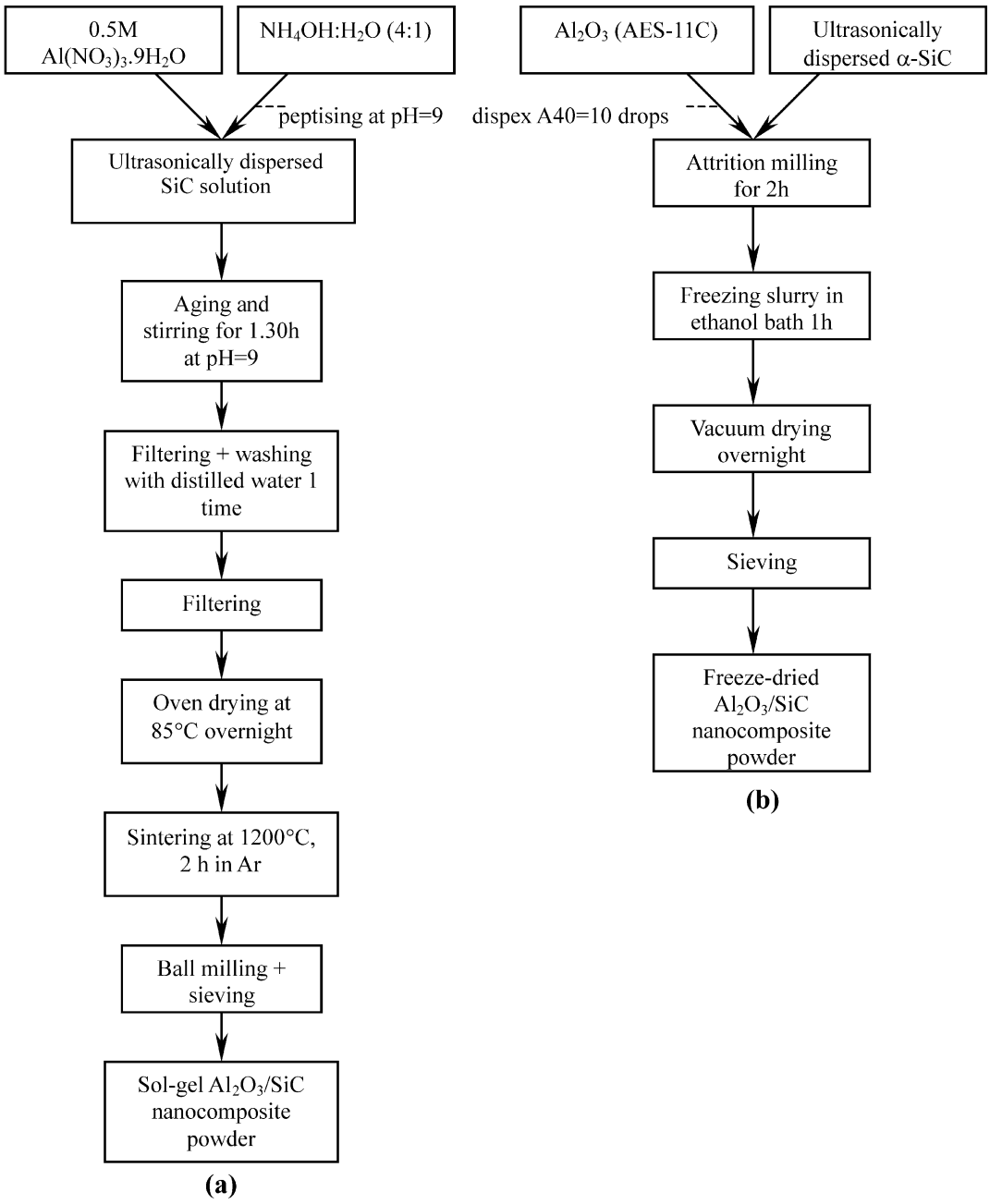

Fig. 1. Processing procedure chats for (a) sol-gel Al_2O_3/SiC nanocomposite powder, and (b) freeze-dried nanocomposite powder.

bond coat prior to the nanocomposite layer in order to further inhibit spalling of the nanocomposite coatings. The Al_2O_3 based coatings were sprayed in five passes of the robot manipulated spray gun over the substrate, to give coating thicknesses of 200–300 μm, on top of a ~160 μm thick CoNiCrAlY bond coat. The Al_2O_3 and Al_2O_3/SiC nanocomposite plasma-sprayed systems are shown schematically in Fig. 2. Plasma spray conditions for all the different powders used and resulting coatings (thickness per spray pass, deposition temperature and water-cooled substrate temperature) are given in Tables 1 and 2, respectively. Deposition temperatures were measured by embedding a small K-type thermocouple on the substrate surface and monitoring the temperature as a function of time using a datalogger. Optimum plasma parameters used for each powder were critically considered depending primarily on the successful adhesion of the ceramic coatings to the stainless steel substrates.

2.5. Phase analysis

Phase composition of all starting powders and as-sprayed plasma-sprayed coatings were investigated by

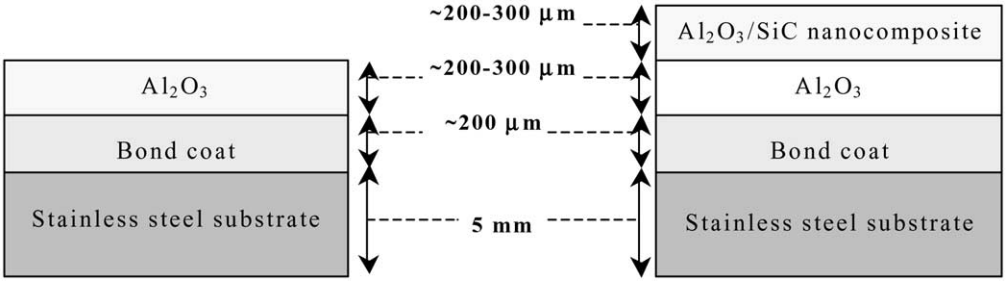

Fig. 2. Schematic diagrams of cross-sectional Al_2O_3 and Al_2O_3/SiC nanocomposite coating systems.

Table 1
Plasma spray processing parameters

Parameters	Bond coat	Al_2O_3[a]	SG45[b]	SG4563[c]	FD[d]
Arc current (A)	719	719	719	719	719
Arc voltage (V)	72	62	63	65	66
Gas flow rate					
Ar (primary) (slpm)	50	40	40	40	35
H_2 (secondary (slpm)	7	4	5	5	7
Powder feed rate (gs^{-1})	0.51	0.32	0.34	0.34	0.36
Powder carrier gas flow rate: Ar (slpm)	1.6	1.9	1.9	1.9	1.9
Chamber pressure (mbar)	60	200	200	200	250
Spray distance (gun-to-substrate) (mm)	270	250	270	240	250

[a] Commercial Al_2O_3.
[b] Sol-gel powder: $\phi < 45$ μm.
[c] Sol-gel powder: $63 < \phi < 45$ μm.
[d] Freeze-dried Al_2O_3 and Al_2O_3/SiC powders.

XRD using a Philips PW1729 diffractometer with CuKα_1 radiation. Solid-state ^{27}Al and ^{29}Si NMR spectroscopy was also used to characterise the phases present. ^{27}Al NMR spectra were obtained on a Chemagnetics Infinity 600 spectrometer, acquired at a magnetic field strength of 14.1 T with a 3.2 mm high-speed MAS probe spun at 18 kHz. The experiments were recorded using a 15° pulse of 0.5 μs and a recycle time of 1 s. The spectra were referenced to the secondary standard of the AlO_6 resource of $Y_3Al_5O_{12}$ at 0.7 ppm. The ^{29}Si NMR spectra were acquired at 7 T using a Bruker spectrometer and a 7 mm MAS probe spun at 3.5 kHz. The experiments were recorded using a 30° pulse of 2 μs and a recycle time of 15–25 s. The spectra were referenced to tetramethylsilane (TMS).

2.6. Microstructure

Microstructural investigation was carried out on coating surfaces, polished cross-sections and manually broken fractured surfaces. As-sprayed coatings were sectioned with a low speed diamond saw, mounted in hot-resin, followed by grinding and polishing, ending with a polish in a 0.06 μm colloidal silica slurry. All specimens were investigated using a Hitachi S520 SEM.

2.7. Porosity

Area percentage porosity of each coating cross-section was measured by optical microscopy and image analysis. Areas were selected with minimal splat/grain pullout during mechanical polishing and a minimum of 15 different measurement areas for each specimen were averaged.

2.8. Surface roughness

Surface roughness traces of the as-sprayed coatings were obtained using a contact type stylus profilometer (Rank Taylor Hobson Surtronic 3+, Leicester, UK), and then solfware analysed (ST3PL.EXE, RTH). Once again, at least 15 different areas of as-sprayed coating

Table 2
Substrate water-cooling temperature (T_{sw}), deposition temperature (T_d), and coating thickness per spraying pass (t_c)

Deposit results	Bond coat	Al_2O_3	SG45	SG4563	FD
T_{sw} (°C)	–	56	48	54	–
T_d (°C)	800	516	415	–	551
t_c/pass (μm)	14	60	70	66	38

surface were measured and the average R_a surface roughness and standard deviation calculated.

3. Results

3.1. Powder microstructure

Fig. 3 shows the particle size distributions of the powders. The commercial Amdry6060 Al_2O_3 had a relatively narrow monomodel particle diameter distribution with a mean particle diameter of 28 μm. The particle diameter distribution is substantially broadened for SG4563, SG45 and FD45 powders, with mean particle diameters of 58.3, 26.6 and 10.4 μm, respectively. These powders also showed mixed mode distributions to varying extents. Fig. 3 also shows that attempts to sieve the in-house powders into narrow size ranges were less successful than hoped. It is likely that significant deviations from spherical as well as agglomeration of particles caused inaccuracies in both sieving and laser diffraction measurement. These characteristics are shown in Fig. 4. Fig. 4(a) shows the Amdry6060 Al_2O_3 powder which was prepared by fusing and crushing, and consequently had an angular, blocky morphology of dense solid particles. This powder had good flowability from the powder hoppers to the plasma gun. Fig. 4(b) shows that the in-house sol-gel Al_2O_3/SiC powder comprised individual solid 45–63 μm particles but with a substantial fraction of much small particles <20 μm. This powder had poorer flowability compared to the Amdry6060 Al_2O_3. Fig. 4(c) shows the agglomerated particles characteristic of the freeze-dried powders, with a combination of solid, blocky particles, plate-like particles and a fraction of particles <20 μm. Again, there was a relatively wide particle size distribution, with some particles of a high aspect ratio and consequently; this powder had the poorest flowability.

3.2. Powder and coating phase analysis

3.2.1. X-ray diffractometry (XRD)

Fig. 5(a) and (b) show XRD traces of the Amdry6060 Al_2O_3 as-received powder and the resulting as-sprayed coating, respectively. The as-supplied powder comprised the equilibrium α-Al_2O_3 phase. However, additional phases in the as-sprayed coating were γ- and δ-Al_2O_3, and now with an apparent minority of α-Al_2O_3. Fig. 6 (a) is an XRD trace of the as-precipitated sol-gel Al_2O_3/SiC nanocomposite powder which consisted of boehmite (AlOOH) and SiC. Fig. 6(b) is the XRD trace of the powder after calcining at 1200 °C/2 h in Ar atmosphere showing a combination of α-Al_2O_3 transformed from AlOOH during high temperature calcination process, α-SiC, and a minority phase matching to aluminosilicate ($Al_2O_3 \cdot xSiO_2$). After plasma spraying in Fig. 6(c), α-SiC, γ- and α-Al_2O_3 were present. Fig. 7(a) shows an XRD trace of the freeze-dried Al_2O_3 powder consisting entirely of α-Al_2O_3. After spraying, the coating also contained γ-Al_2O_3 as shown in Fig. 7(b). Fig. 7(c) and (d) are the XRD traces for freeze-dried Al_2O_3/10 vol.% SiC nanocomposite powder and its coating, respectively. The freeze-dried Al_2O_3/10 vol.% SiC powder had mainly α-Al_2O_3 together with SiC phases, whereas the coating

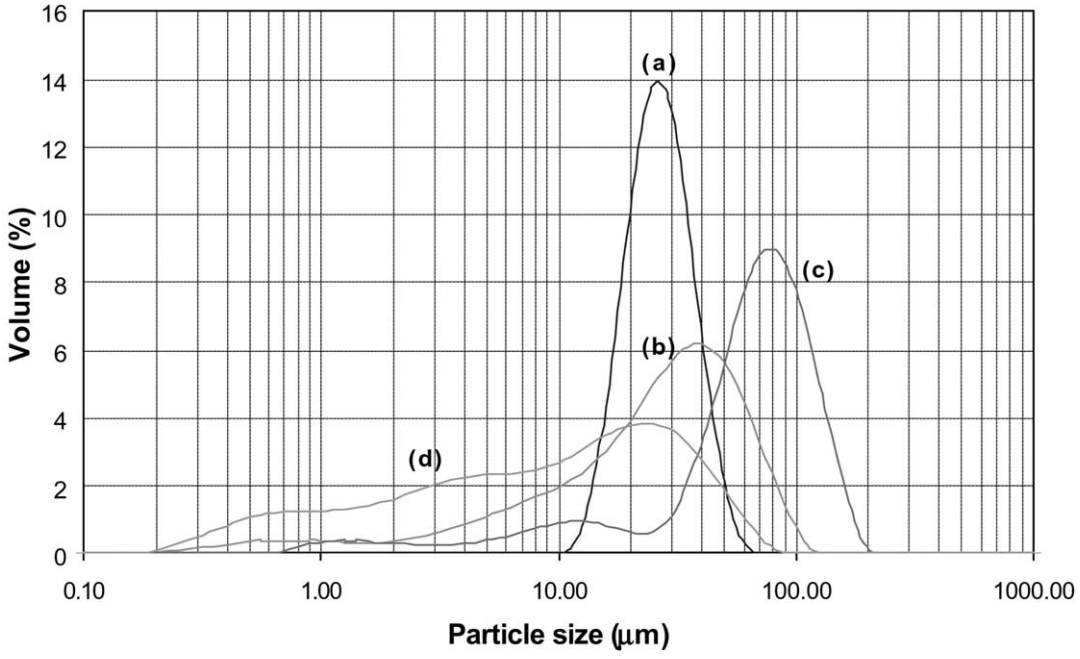

Fig. 3. Particle size distribution of feedstock powders used for low pressure plasma spraying: (a) commercial Al_2O_3 (Amdry6060), (b) sol-gel Al_2O_3/SiC (SG45), (c) sol-gel Al_2O_3/SiC (SG4563) and (d) freeze-dried powder (FD45).

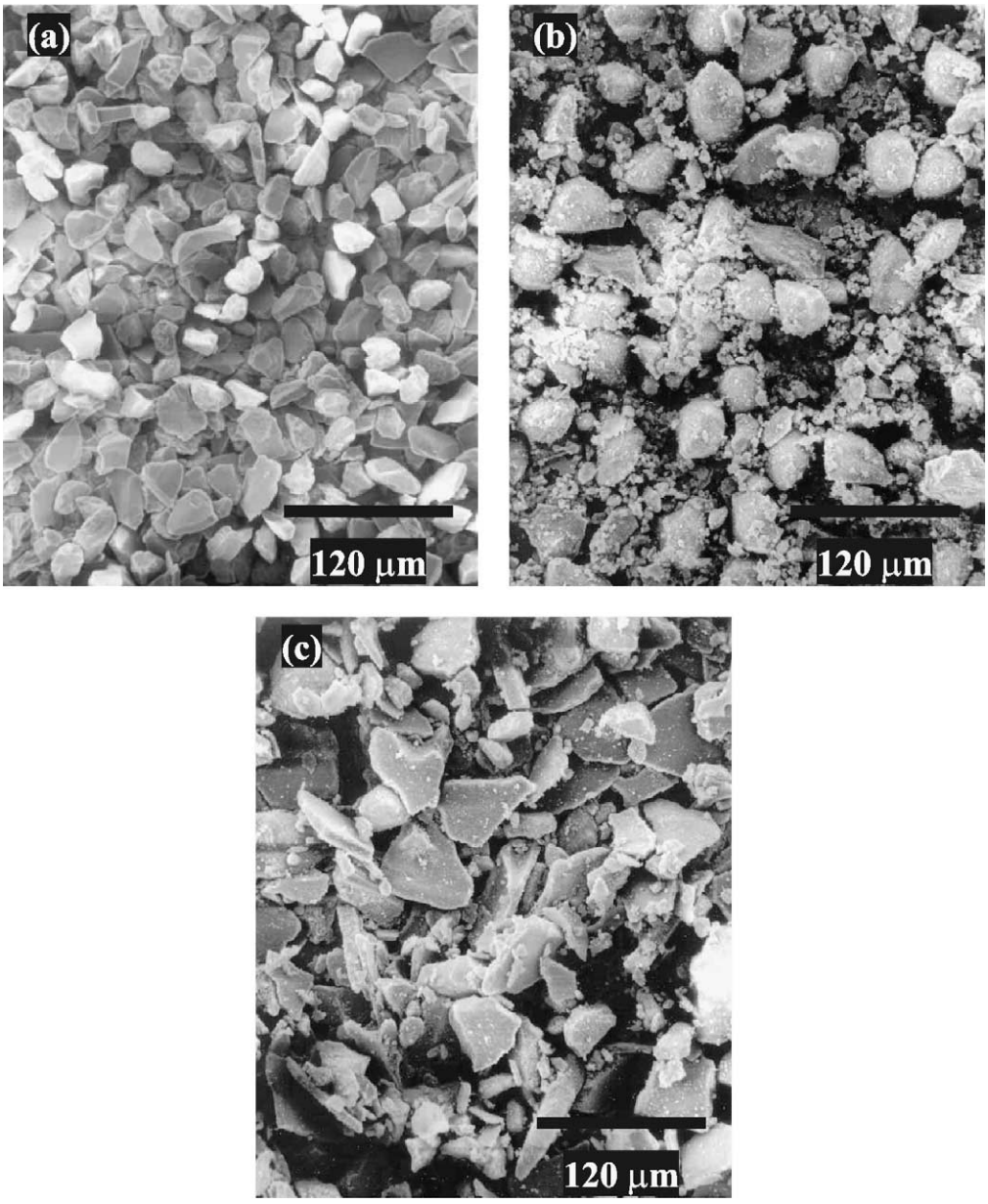

Fig. 4. Scanning electron micrographs of feedstock powders: (a) commercial Amdry6060 Al_2O_3, (b) sol-gel Al_2O_3/SiC, and (c) freeze-dried Al_2O_3.

again included γ-Al_2O_3. Similar behaviour was also shown by the freeze-dried Al_2O_3/20 vol.% SiC powder [Fig. 7(e)] and its coating [Fig. 7(f)]. Table 3 summarises the phases present in all powders and coatings observed by XRD.

3.2.2. Nuclear magnetic resonance: ^{27}Al and ^{29}Si NMR

Fig. 8 shows ^{27}Al NMR spectra of powders and plasma sprayed coatings. Fig. 8(A-a) is the spectrum of Amdry6060 Al_2O_3 powder, showing an intense peak at $\approx +14$ ppm which can be entirely attributed to octahedral AlO_6 alumina (α-Al_2O_3), i.e. O atoms in approximate hexagonal close packing (hcp) with Al atoms in 2/3 of the octahedral sites.[17] The ^{27}Al NMR spectrum of the Amdry6060 Al_2O_3 coating is shown in Fig. 8(A-b), with an octahedral AlO_6 peak at $\approx +12$ ppm and tetrahedral AlO_4 peak (γ-, δ-Al_2O_3) at $+66$ ppm. Fig. 8(B-a) shows the ^{27}Al NMR spectrum of the calcined sol-gel Al_2O_3/SiC powder, again indicating AlO_6 and AlO_4 peaks. Both of these peaks were detected in the sol-gel Al_2O_3/SiC coating shown in Fig. 8(B-b). However, there was a minor peak of the less common five-coordinated AlO_5 group resonating between AlO_6 and AlO_4 at $+34$ ppm, and which was identified as ρ-Al_2O_3.[18] Fig. 8(C-abc) are respectively ^{27}Al NMR spectra of freeze-dried Al_2O_3, Al_2O_3/10 vol.%SiC and Al_2O_3/20 vol.% SiC nanocomposite powders which also showed a single AlO_6 peak at $\approx +14$ ppm. The ^{27}Al NMR spectra of the

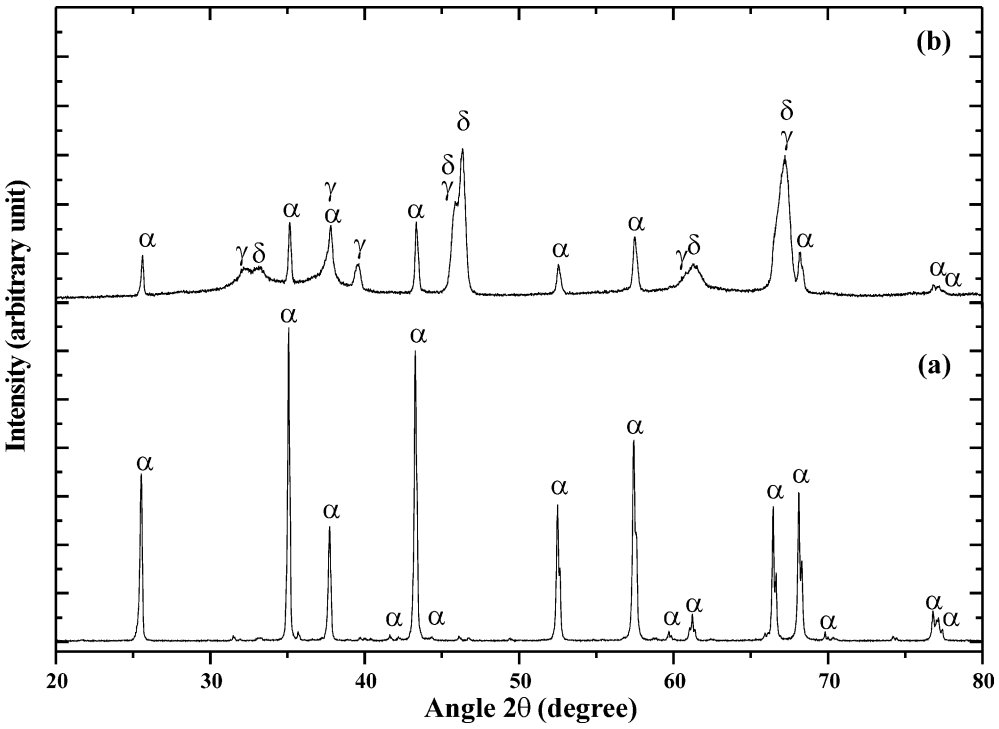

Fig. 5. X-ray diffraction traces: (a) commercial Amdry6060 Al_2O_3 powder, and (b) its as-sprayed coating (α = stable Al_2O_3 phase, and γ-, δ- = metastable Al_2O_3 phases).

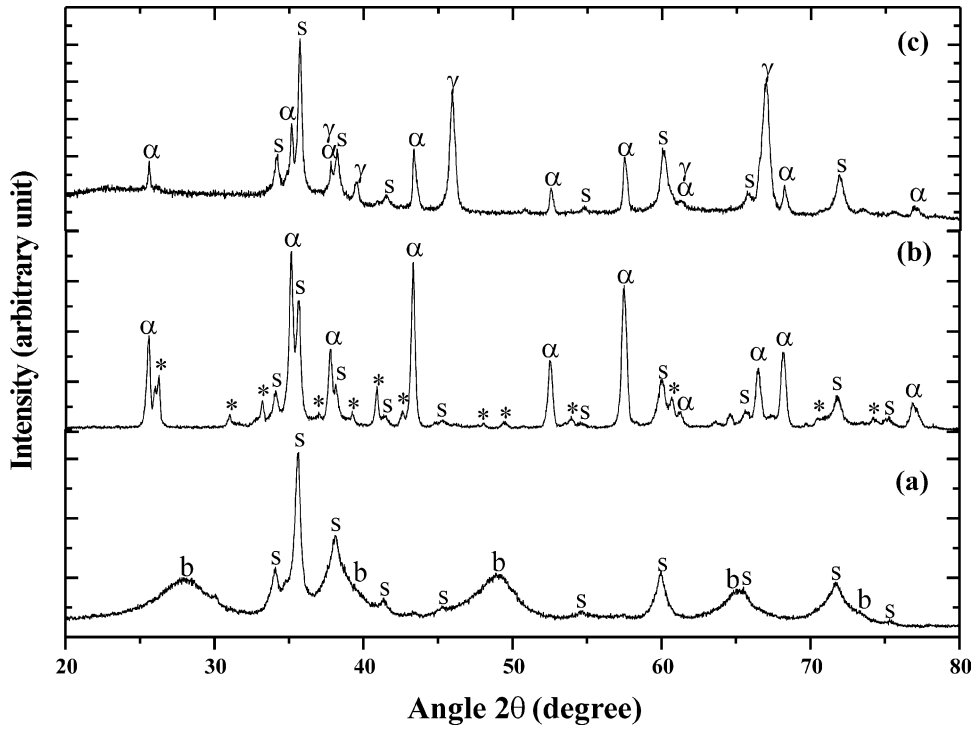

Fig. 6. X-ray diffraction traces: (a) as-precipitated sol-gel Al_2O_3/SiC powder, (b) powder calcined at 1200C in Ar for 2 h, and (c) its as-sprayed coating (b = boemite, s = SiC, * = aluminosilicate, α = stable Al_2O_3 phase, and γ = metastable Al_2O_3 phases).

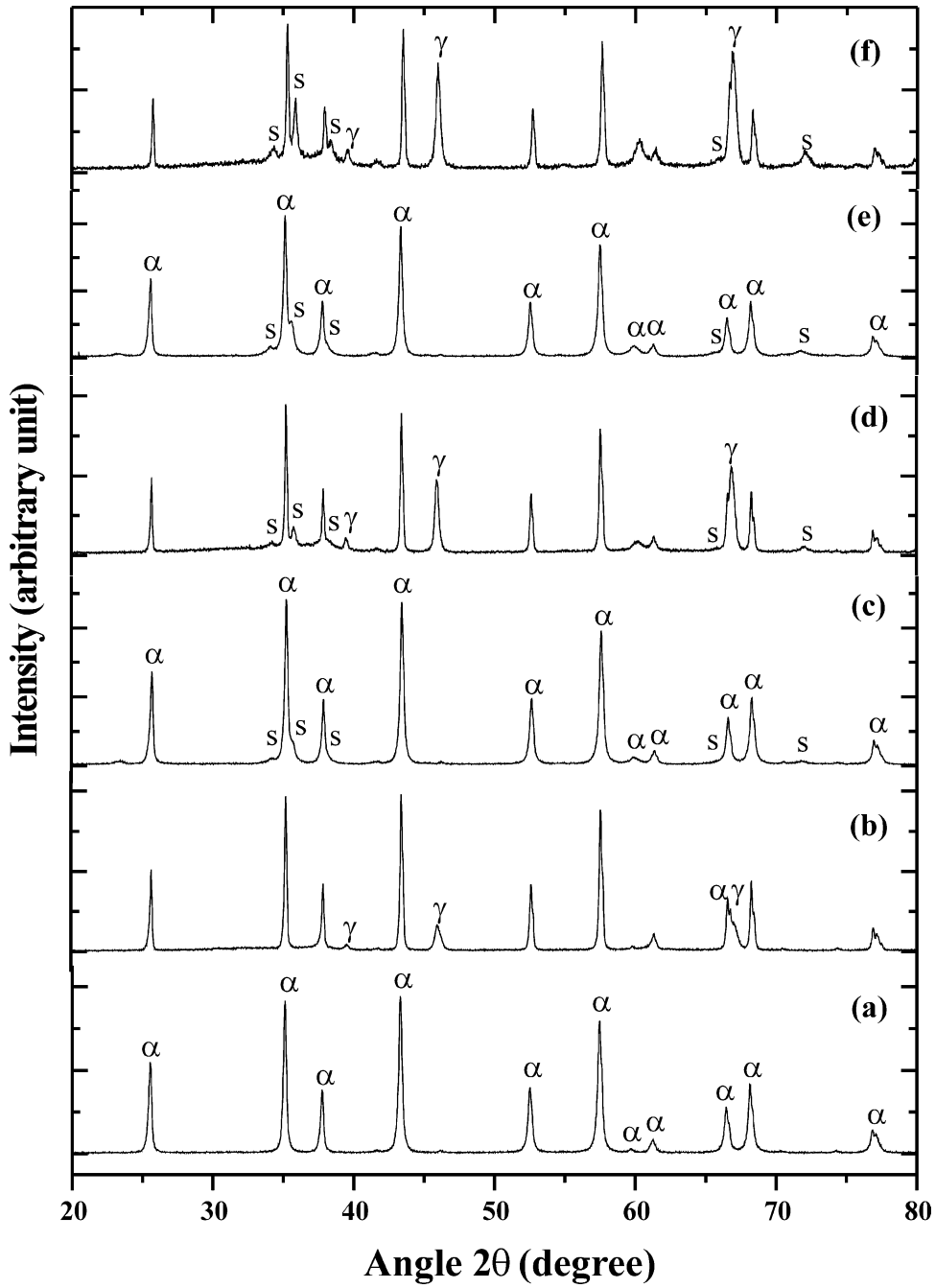

Fig. 7. X-ray diffraction traces: (a) and (b) are Al_2O_3 powder and its coating; (c) and (d) are Al_2O_3/10 vol.% SiC powder and its coating; (e) and (f) are Al_2O_3/20 vol.% SiC powder and its coating (s = SiC, α = stable Al_2O_3 phase, and γ = metastable Al_2O_3 phases). Unmarked peaks represent α-Al_2O_3 phase.

corresponding coatings are shown in Fig. 8(C-def), and again, spectra were dominated by AlO_6 (at ≈ + 14 ppm) and AlO_4 (at ≈ + 67 ppm) peaks.

Fig. 9 shows ^{29}Si NMR spectra of sol-gel Al_2O_3/SiC, freeze-dried Al_2O_3/10 vol.% SiC and Al_2O_3/20 vol.% SiC nanocomposite powders and their plasma-sprayed coatings. The ^{29}Si NMR spectrum of calcined sol-gel Al_2O_3/SiC powder in Fig. 9(A-a) indicated not only the presence of α-SiC (i.e. peaks at −10, −16.2 and −20.8 ppm) and aluminosilicate (i.e. peak at −108 ppm), previously detected by XRD, but also a peak associated with silica at −79 ppm. The relatively broad aluminosilicate ($Al_2O_3 \cdot xSiO_2$) and silica (SiO_2) peaks suggested a tendency towards an amorphous structure. Fig. 9(A-b) shows the ^{29}Si NMR spectrum of the resulting coating, which shows the intense peaks of α-SiC, but now without any indication of either aluminosilicate or silica phases. The ^{29}Si NMR spectrum

Table 3
Summary of phases present in commercial Amdry6060 Al_2O_3, sol-gel Al_2O_3/SiC, freeze-dried Al_2O_3 and freeze-dried Al_2O_3/SiC powders and the as-received coatings detected by XRD

Materials	Powder phases	Coating phases
Amdry6060 Al_2O_3	$\underline{\alpha}$-Al_2O_3	$\alpha + \underline{\gamma} + \delta$-$Al_2O_3$
Sol-gel	$\underline{\alpha}$-Al_2O_3 + SiC + $Al_2O_3 \cdot xSiO_2$	$\alpha + \underline{\gamma}$-$Al_2O_3$ + SiC
Freeze-dried Al_2O_3	$\underline{\alpha}$-Al_2O_3	$\underline{\alpha} + \gamma$-$Al_2O_3$
Freeze-dried Al_2O_3/SiC	$\underline{\alpha}$-Al_2O_3 + SiC	$\underline{\alpha} + \gamma$-$Al_2O_3$ + SiC

Underlining indicates the major phase.

of the freeze-dried Al_2O_3/10 vol.% SiC powder and its coating are shown in Fig. 9(B-a) and 9(B-b) respectively and in both cases only peaks indicating α-SiC were detected, and similarly for the freeze-dried Al_2O_3/20 vol.% SiC powder [Fig. 9(B-c)] and its coating [Fig. 9(B-d)]. Table 4 summarises the phases present in all types of powder and coating observed by both ^{27}Al and ^{29}Si NMR.

3.3. Coating microstructure

Figs. 10–12 each show a set of SEM micrographs of the coating surface, coating cross-section and deliberately fractured coating, respectively, for each of the (a) Amdry6060 Al_2O_3, (b) sol-gel Al_2O_3/SiC <45 μm (SG45), (c) sol-gel Al_2O_3/SiC 45–63 μm (SG4563) and (d) freeze-dried Al_2O_3 <45 μm coatings.

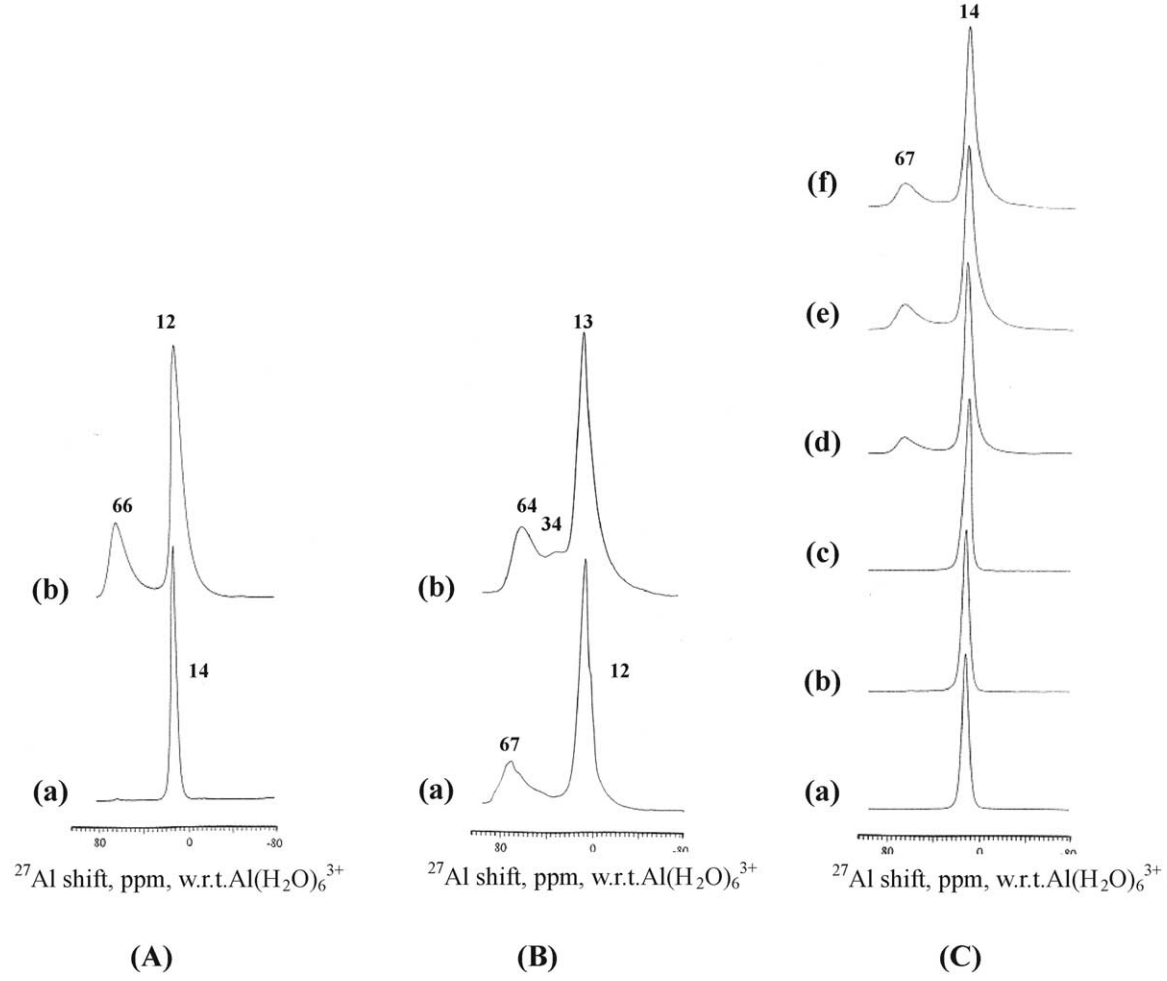

Fig. 8. ^{27}Al NMR: (A) commercial Amdry6060 Al_2O_3; (a) = powder and (b) = coating, (B) sol-gel Al_2O_3/SiC; (a) = powder calcined at 1200 °C for 2 h in Ar and (b) = as-sprayed coating and (C) freeze-dried Al_2O_3/SiC; (a) = 0 vol.% SiC powder, (b) = 10 vol.% SiC powder, (c) = 20 vol.% SiC powder, (d) = 0 vol.% SiC coating, (e) = 10 vol.% SiC coating and (f) = 20 vol.% SiC coating.

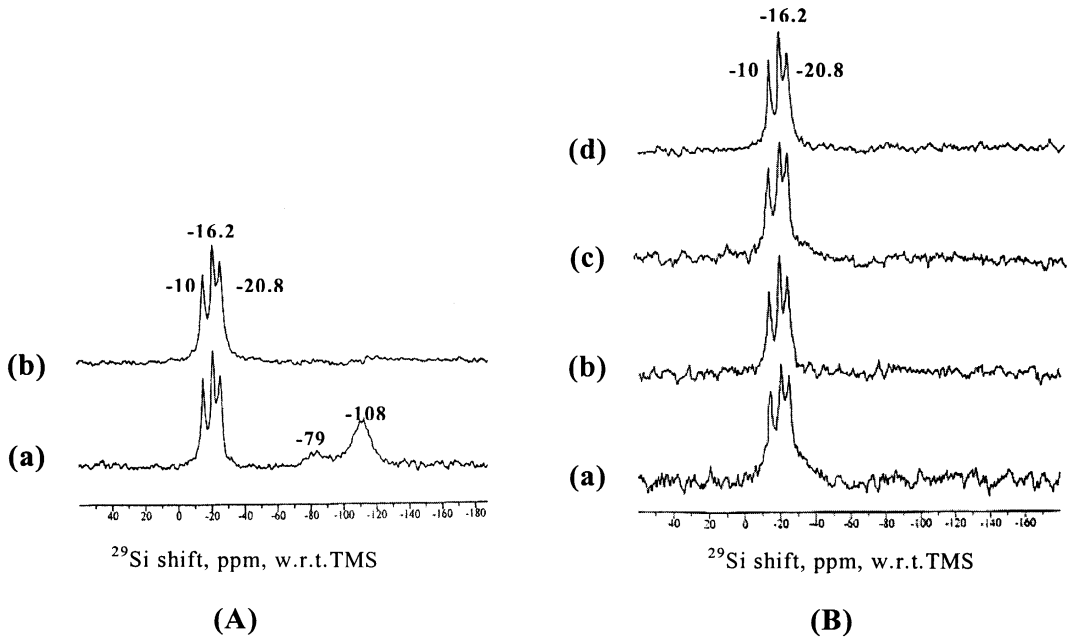

Fig. 9. ^{29}Si NMR: (A) sol-gel Al_2O_3/SiC; (a) = powder calcined at 1200 °C for 2 h in Ar and (b) = as-sprayed coating, and (B) freeze-dried Al_2O_3/SiC; (a) = 10 vol.% SiC powder, (b) = 10 vol.% SiC coating, (c) = 20 vol.% SiC powder, and (d) = 20 vol.% SiC coating.

Fig. 10(a) shows that the Amdry6060 Al_2O_3 powder had the highest degree of melting, as evidenced by the homogenous pancake-like splats on the coating surface. A network of microcracks was formed inside the individual Al_2O_3 splats. Fig. 10(b) shows the surface of the SG45 coating comprising splats from impacting droplets at different degrees of melting, and some relatively large pores up to 1 μm inside the splats. Fig. 10(c) shows the surface of SG4563 coating which had a similar surface appearance to SG45, but with a generally larger splat size. Microcracking was again evident but to a lesser extent than for Amdry6060 or SG4563. Fig. 10(d) shows an example of the freeze-dried coating surface. Splats were again evident but with a large amount of small unmolten particles apparently broken away from the agglomerates during flight in the plasma flame. A highly porous foam-like structure [top-left corner in the Fig. 10(d)] was occasionally present.

Fig. 11(a)–(d) show the coating cross-sections, and which in general confirm the greater extent of particle melting for Amdry6060 Al_2O_3 in comparison to sol-gel and freeze-dried in-house powders. In Fig. 11(a), the Amdry6060 coating shows the characteristic lamellae microstructure in cross-section, but with a lower area fraction of pores in comparison with sol-gel and freeze-dried coatings, despite careful optimisation of the processing parameters for each powder. Fig. 11(b) is the cross-section of the SG45 coating which shows not only the lamellae microstructure and a slightly increase in porosity but also flaws because of particle pull-out during mechanical polishing. The cross-sectional microstructure of SG4563 in Fig. 11(c) contained pores within splats, and a well-defined lamellae structure separated by thin layer of voids resulting from poor interlamellar contact. There were also many incompletely molten particles trapped between well-molten particles because a fraction of the feedstock powder comprised particles too large to be melted in the plasma. Again, particle pull-out was problematical in the SG4563 coatings. The cross-sectional microstructure of FD45 coating in Fig. 11(d) was similarly to the microstructure of SG4563, but contained finer splat lamellae, a higher fraction of interlamellar voids, porosity and pullout because of weak bonding of incompletely molten agglomerates.

Fig. 12(a) is the fractured surface of the Amdry6060 Al_2O_3 coating, again clearly showing the well-defined lamellae structure, with a lamellae thickness of 2–3 μm and small pores between splat layers. The lamellar thickness increased as the feedstock particle size increased, as shown by the fracture surface of SG45 (lamellar thickness 4–5 μm) and SG4563 (lamellar thickness 4–10 μm) in Fig. 12(b) and (c), respectively. Both SG45 and SG4563 coatings had pores $\geqslant$1 μm inside splats, and these pores probably originated from pores in the powders after calcination. Fig. 12(d) shows the fractured surface of the FD45 coating which comprised agglomerates of partially melted particles and splats. It was not possible to evaluate splat thickness because of the complexity of the microstructure.

Table 4
Summary of phases present in commercial Amdry6060 Al_2O_3, sol-gel Al_2O_3/SiC, freeze-dried Al_2O_3 and freeze-dried Al_2O_3/SiC powders and the as-received coatings detected by ^{27}Al and ^{29}Si NMR

Materials	Powder phases	Coating phases
Amdry6060 Al_2O_3	$\underline{AlO_6}$	$AlO_6 + \underline{AlO_4}$
Sol-gel	$\underline{AlO_6} + A1O_4 + SiC + SiO_2 + Al_2O_3 \cdot xSiO_2$	$AlO_6 + \underline{AlO_5} + \underline{AlO_4} + SiC$
Freeze-dried Al_2O_3	$\underline{AlO_6}$	$\underline{AlO_6} + AlO_4$
Freeze dried Al_2O_3/SIC	$\underline{AlO_6} + SiC$	$\underline{AlO_6} + AlO_4 + SiC$

Underlining indicates the major phase.

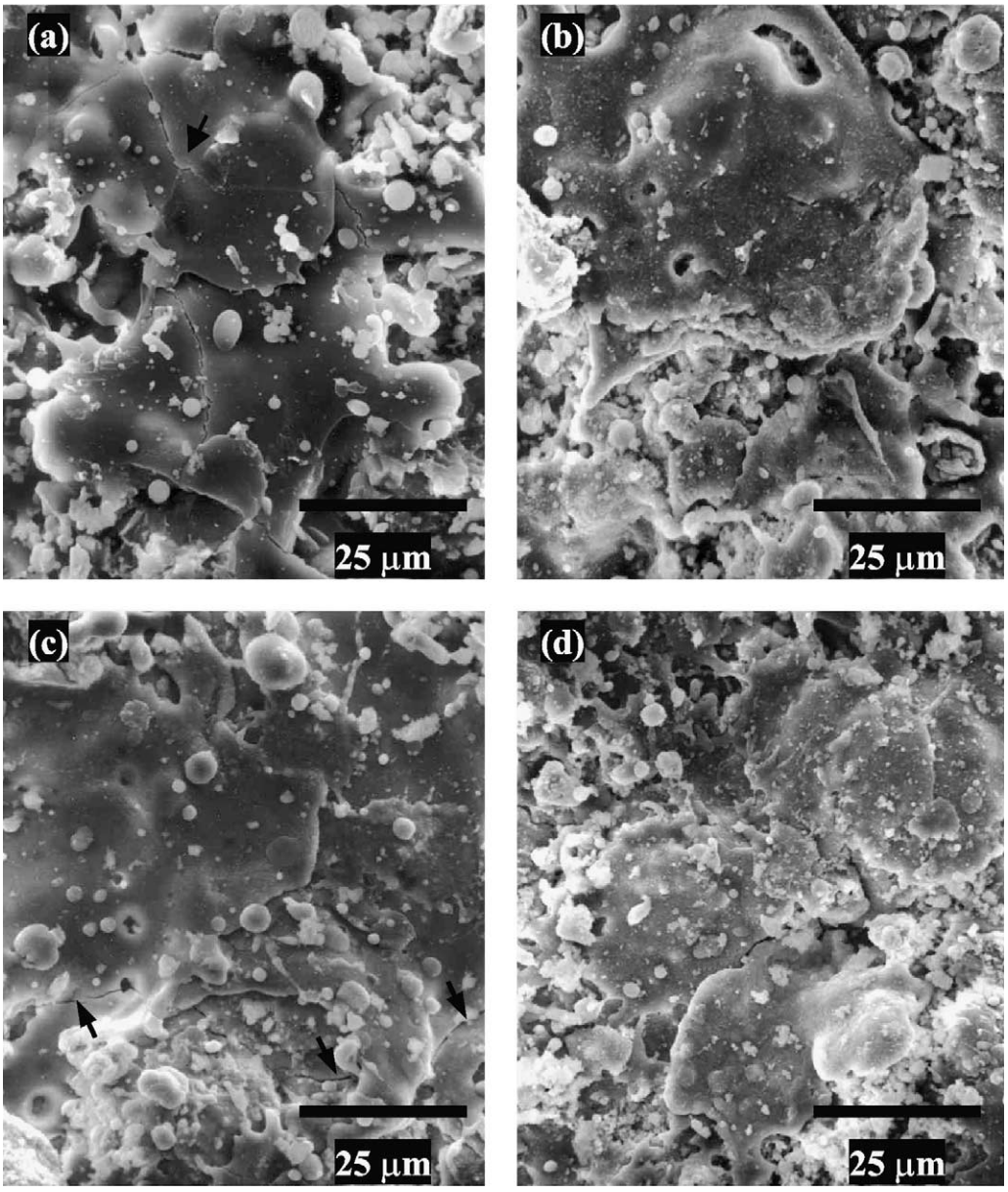

Fig. 10. Scanning electron micrographs of as-sprayed coating surfaces: (a) commercial Amdry6060 Al_2O_3, (b) sol-gel Al_2O_3/SiC (SG45), (c) sol-gel Al_2O_3/SiC (SG4563), and (d) freeze-dried Al_2O_3/SiC (FD45) [an arrow in (a) indicates a microcrack network, arrows in (c) indicate individual microcracks].

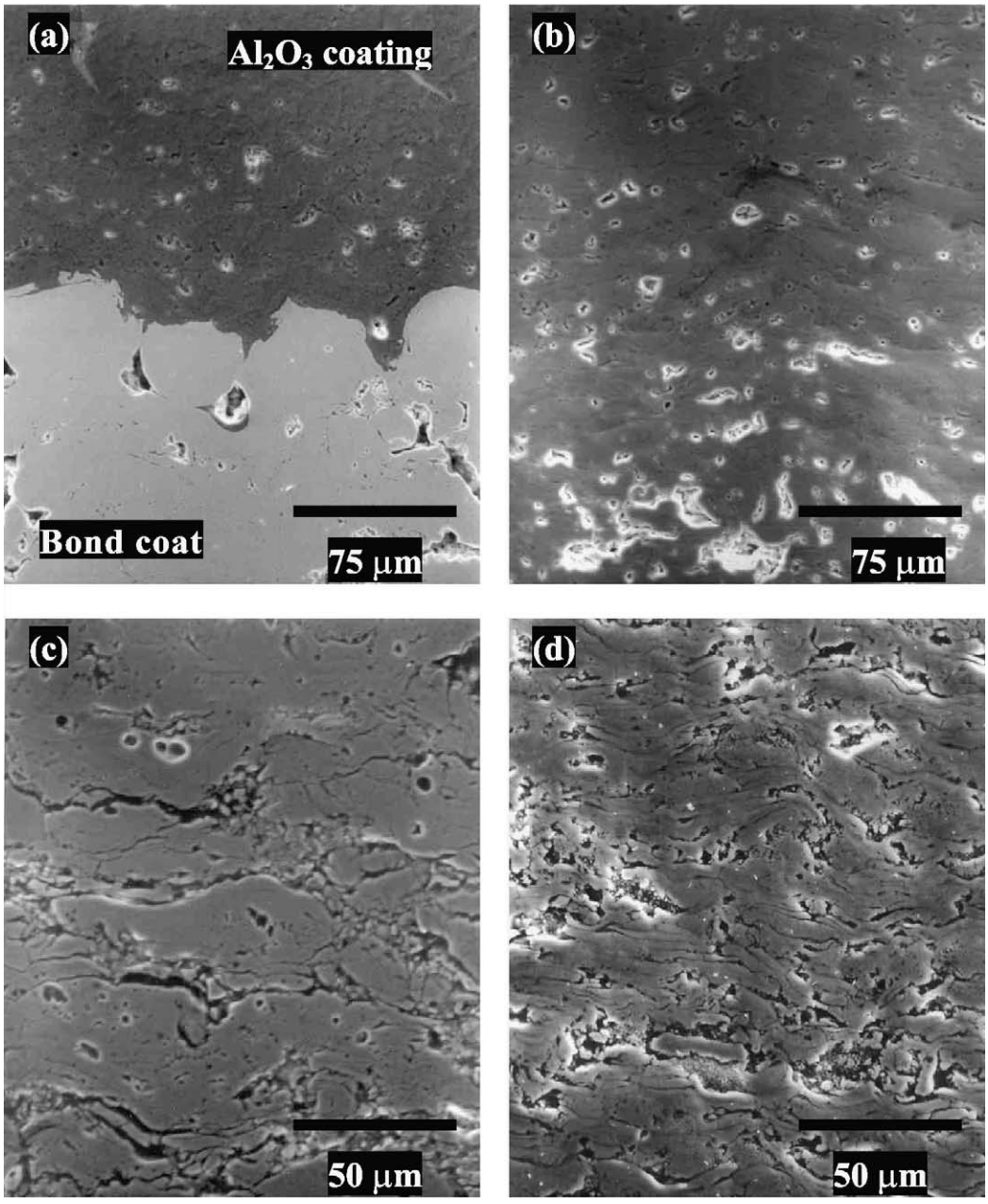

Fig. 11. Scanning electron micrographs of polished cross-sections: (a) commercial Amdry6060 Al_2O_3, (b) sol-gel Al_2O_3/SiC (SG45), (c) sol-gel Al_2O_3/SiC (SG4563), and (d) freeze-dried Al_2O_3/SiC (FD45).

3.4. Porosity and surface roughness analysis

Fig. 13 shows the average area percentage of porosity for each coating cross-section. The Amdry6060 Al_2O_3 coating had the lowest porosity of ≈7%, and similar to SG45 coating. The high fraction of interlamellar voids and pores observed in the SG4563 and FD45 coatings increased porosity to ≈8 and ≈10% respectively. The porosity of freeze-dried coatings was unaffected by the vol.% SiC.

Fig. 14 shows the average surface roughness (R_a) for each coating. The larger feedstock particle diameter, then the rougher the coating surface with $R_a(SG4563) > R_a(SG45) > R_a(Amdry6060\ Al_2O_3)$ (11.5 > 7.9 > 5.4 μm). The surface roughness of freeze-dried Al_2O_3, Al_2O_3/10 vol.% SiC and Al_2O_3/20 vol.% SiC coatings were approximately equal.

4. Discussion

Sol-gel processing involves the precipitation of metal oxide particles from solution and is used widely to produce ceramics of small particle sizes with controlled chemical purity and crystallinity. $Al(NO_3)_3{\cdot}9H_2O$, NH_4OH and an excess H_2O are used to produce boehmite

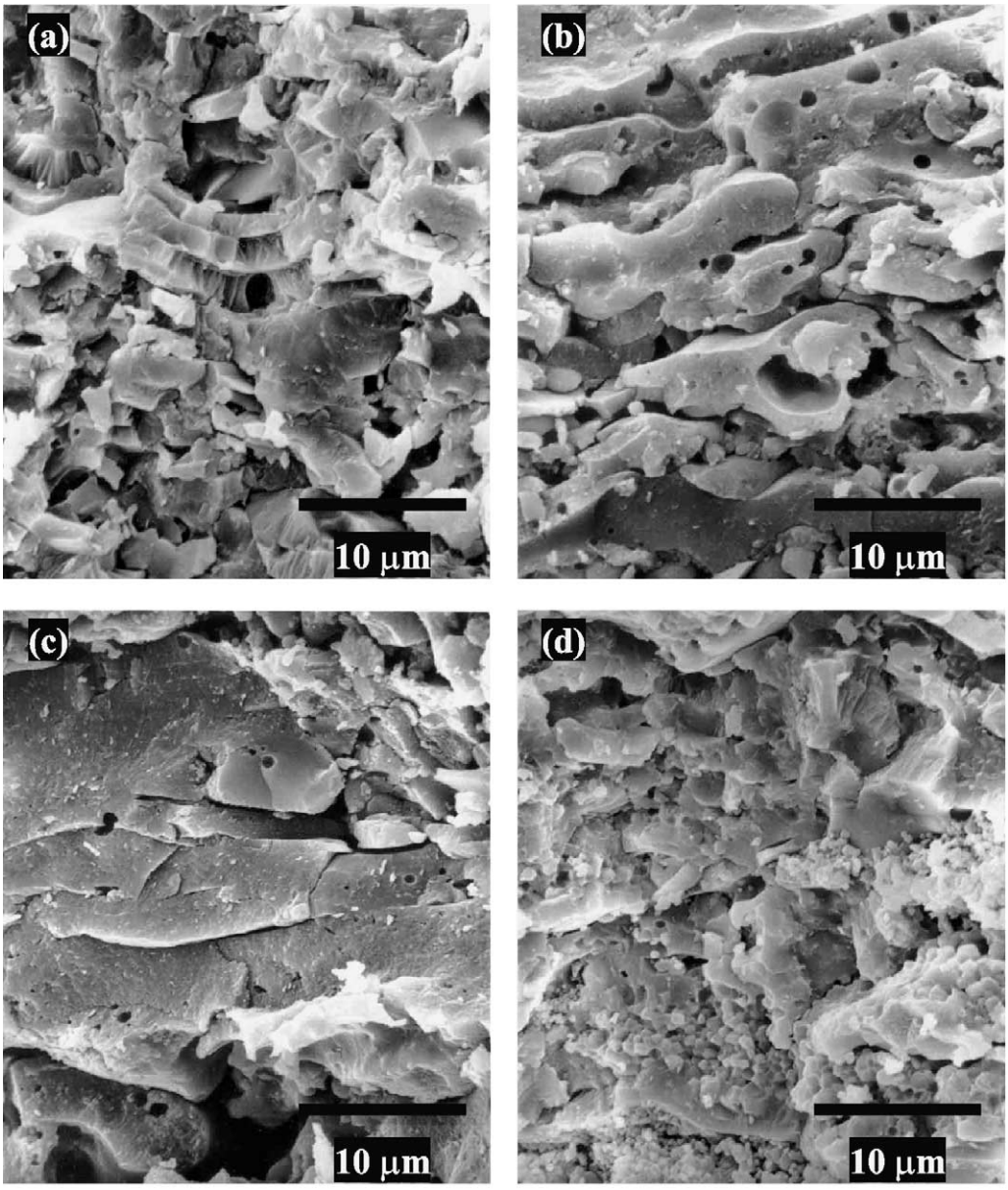

Fig. 12. Scanning electron micrographs of fractured cross-sections: (a) commercial Amdry6060 Al_2O_3, (b) sol-gel Al_2O_3/SiC (SG45), (c) sol-gel Al_2O_3/SiC (SG4563), and (d) freeze-dried Al_2O_3/SiC (FD45).

(AlOOH) which is generally accepted as the starting material for Al_2O_3[19–21] according to:

$$Al(NO_3)_3 + 3NH_4OH + \times H_2O \xrightarrow{T_R, pH \approx 9} 3NH_4NO_3 + Al(OH)_3 + xH_2O$$

$$3NH_4NO_3 + Al(OH)_3 + xH_2O \xrightarrow{\text{washed, filtered}} Al(OH)_3$$

$$Al(OH)_3 \xrightarrow{\text{dehydrated}} AlOOH + H_2O$$

AlOOH transforms into stable α-Al_2O_3 via metastable γ-, δ-, and θ-Al_2O_3 transition phases, in order of increasing temperature.[18] The thermal transformation sequence of boehmite to α results in a change of the O atom packing from cubic close pack (ccp) to hexagonal close pack (hcp), with Al atoms in octahedral sites in both cases. The tetrahedral γ- and δ-Al_2O_3 are both spinel-related with ccp oxygen,[17] and the proportion of tetrahedrally coordinated Al atoms increases through the sequence γ, δ and θ. These metastable transitional forms of alumina are not present in the XRD traces of the calcined sol-gel Al_2O_3/SiC powder as shown in Fig. 6(b). However, NMR (^{27}Al) proved to be more sensitive to minority phases indicating the presence of either γ-, δ- and θ-Al_2O_3 as shown in Fig. 8(B). ^{29}Si NMR spectra of the calcined sol-gel Al_2O_3/SiC powder in Fig. 9(A-a) indicates not only the presence of α-SiC and $Al_2O_3 \cdot xSiO_2$ as detected by XRD, but also a peak associated with SiO_2 not detected by XRD. Although calcination of the sol-gel Al_2O_3/SiC powder takes place

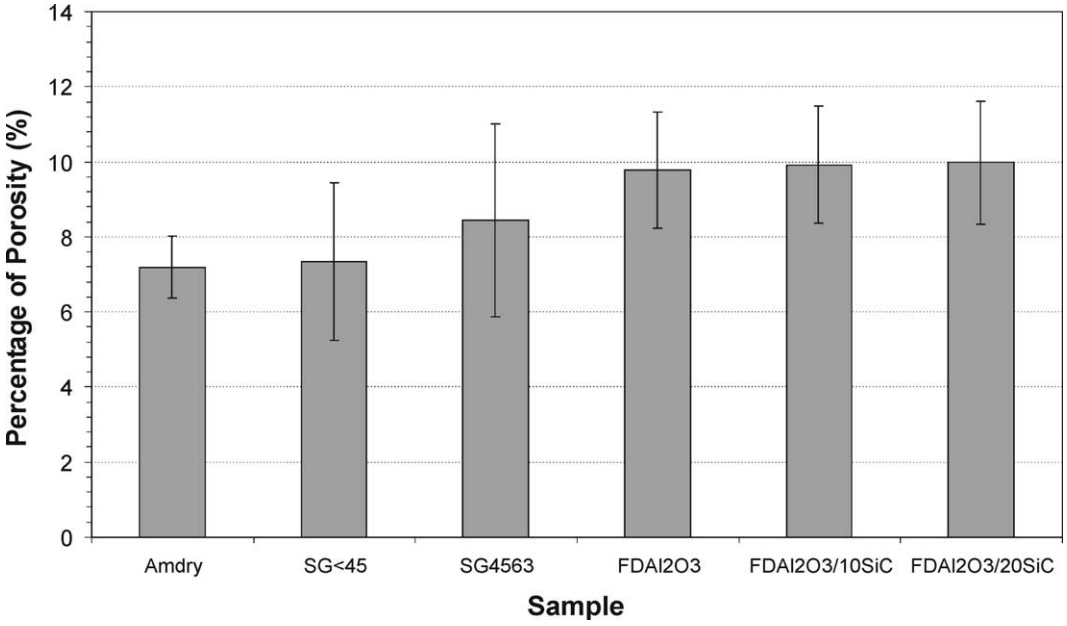

Fig. 13. Percentage area porosity of polished cross-sectional coatings calculated using an image analysis.

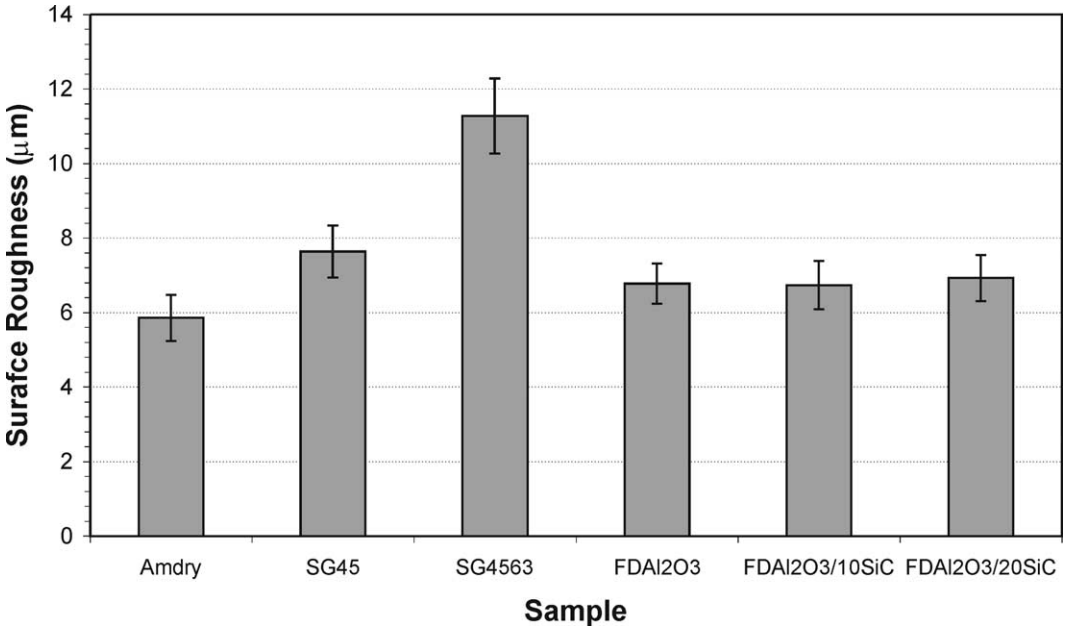

Fig. 14. Surface roughness of all as-plasma sprayed coatings measured using a contact type stylus profiler.

in an Ar atmosphere, it is possible that sufficient O either from an evaporation of the Al_2O_3 matrix or from ingress of atmosphere reacted with SiC to form a minor fraction of $Al_2O_3{\cdot}xSiO_2$ and SiO_2.

$$SiC_{(s)} + 2O_{2(g)} \rightarrow SiO_{2(s)} + CO_{2(g)} \uparrow$$
$$SiC_{(s)} + 1.5O_{2(g)} \rightarrow SiO_{2(s)} + CO_{(g)} \uparrow$$
$$Al_2O_{3(s)} + \times SiO_{2(s)} \rightarrow Al_2O_3{\cdot}xSiO_{2(s)}$$

Both peaks are relatively broad which is consistent with an amorphous-like structure.

Phase analysis of all as-sprayed coatings by XRD and NMR shows that the materials comprise a combination of stable and metastable Al_2O_3 phases. XRD traces of the monolithic Al_2O_3 show a combination of γ-, δ- and α-Al_2O_3. It has been suggested that the metastable γ-Al_2O_3 is always homogeneously nucleated in the rapid quenching of completely molten droplets because of the critical free energy for nucleation from the liquid is less that that of α-Al_2O_3.[6] The metastable δ-Al_2O_3 in the coating arises from the transformation of γ-Al_2O_3. In this study, a water-cooled substrate was used which increased the coating cooling rate and therefore, limited

the transformation of γ- to δ-Al_2O_3. The presence of δ-phase may also arise from the reheating of the coating during deposition of subsequent layers, followed by rapid coating cooling when the plasma is moved away again by the robot. α-Al_2O_3 in the coatings arises from a combination of a fraction of unmelted feedstock powder which is entirely composed of α-Al_2O_3, and the continued decomposition of γ-, δ-, and θ-Al_2O_3 transition phases. XRD traces of sol-gel and freeze-dried coatings show a combination of γ- and α-Al_2O_3 but no detectable δ-Al_2O_3. It is therefore suggested that the decomposition of γ- to δ-phase is less progressed in the sol-gel and freeze-dried coatings compared with the Amdry6060 Al_2O_3 coating because of poorer melting and lower temperatures in both the plasma flame and at deposition.

Although the sol-gel and freeze-dried Al_2O_3/SiC nanocomposite powders experience high temperatures of ~5000–25 000 °C in the plasma flame for a short time, XRD and ^{29}Si NMR show that the nanoscale SiC is well-preserved in the final coatings, because of the relatively high thermal stability of α-SiC with T_m = 2200–2700 °C. Furthermore, the amorphous-like SiO_2 and $Al_2O_3{\cdot}xSiO_2$ phases in the calcined sol-gel Al_2O_3/SiC powder are now absent in the sprayed coating. The Al_2O_3–SiO_2 phase diagram shows that at above ~1950 °C, the SiO_2 (T_m = 1734 °C) and mullite-$3Al_2O_3{\cdot}2SiO_2$ (T_m = 1934 °C) become a fully mixed liquid and are apparently unable to reconstitute on rapid solidification.

The formation of the pancake-like splats on all coating surfaces in Fig. 10 indicates droplets of moderate heat content and velocity at impact.[22] Because a large temperature gradient exists across the interface between the flattened liquid droplet splat and substrate (or previously solidified droplet), the thermal contraction of each splat is restrained by the underlying solid, and a microstress distribution is established within the splat. This leads to the formation of microcrack networks inside the individual Amdry6060 Al_2O_3 splats. The sol-gel Al_2O_3/SiC splats had individual microcracks rather than extensive networks. It is hypothesised that the microcracks in the sol-gel Al_2O_3/SiC coatings are prevented from interlinking as a result of higher degree of unmolten/partially molten of feedstock powder. Polished cross-sectional (Fig. 11) and fractured (Fig. 12) microstructures of the sol-gel Al_2O_3/SiC coatings reveals pores (as large as 1 μm) inside each lamellae. These pores are likely those remaining from calcination process of as-precipitated Al_2O_3/SiC sol-gel powder, however, these pores may also derive from the decomposition of unstable SiO_2 and $Al_2O_3{\cdot}xSiO_2$ phases.

Average coating porosity and surface roughness depend on the ability of the plasma to melt the powders and are dependent upon the mean particle size, distribution and morphology. The larger the particle diameter, then the higher the porosity and surface roughness, as shown in Figs. 13 and 14. The broader the particle size distribution, then the higher the porosity, e.g. the agglomerated nature of the freeze-dried powder led to poor flowability, poor melting and relatively high levels of porosity and surface roughness. In all cases, the freeze-dried nanocomposite powders and coatings showed no dependency of microstructure on SiC volume fraction in the range 0–20 vol.%.

5. Conclusions

Al_2O_3/SiC nanocomposite ceramic coatings have been successfully fabricated by LPPS from sol-gel and freeze-dried feedstock powders prepared in-house. After careful optimisation employing substrate water-cooling, nanocomposite coating were well-adhered to stainless steel substrates using CoNiCrAlY and monolithic Al_2O_3 bond coats.

Mean feedstock particle diameter, particle diameter distribution and morphology affected the extent of particle melting in the plasma flame. Powder melting in turn controlled the phases, microstructure, area percentage of porosity and surface roughness of the as-sprayed coating.

Thermal cycling during plasma spraying caused phase changes and decompositions in the feedstock powder. XRD and ^{27}Al NMR showed that α-Al_2O_3 in all starting powders was partially transformed to metastable phases such as γ- and δ- in monolithic Al_2O_3 coatings, and additionally to γ- in the sol-gel and freeze-dried coatings, during plasma spraying. The higher the fraction of coating metastable phases then the better feedstock powder melting. Nanoscale α-SiC in the Al_2O_3/SiC sol-gel and freeze-dried feedstock powders was well-preserved in the as-sprayed coatings. XRD and ^{29}Si NMR showed that after spraying, aluminosilicate and silica phases in the calcined Al_2O_3/SiC sol-gel powders were removed.

Coating microstructures comprised a combination of fully molten and incompletely molten pancake-like splats. The monolithic Al_2O_3 coating indicated the highest degree of powder melting, but with splats that contained microcrack networks because of thermal contraction during cooling. Microcracks were inhibiting in forming extended networks in the nanocomposite coatings because incompletely/partially molten particles led to a less coherent coating.

The larger the particle diameter and the broader the particle diameter distribution, then the higher area percentage of coating porosity and the rougher the resulting surface of the as-sprayed coating.

Although the mechanical properties of the Al_2O_3/SiC nanocomposite coatings have not been mentioned in this paper, the mechanical study of the Al_2O_3/SiC nanocomposite coatings will be further investigated. It has been many reports on mechanical enhancements of

bulk Al_2O_3/SiC nanocomposite over bulk monolithic Al_2O_3.[9–16] The nanocomposite coating should offer significant mechanical improvements in some aspects over the monolithic Al_2O_3 coating as has been found in the bulk materials.

Acknowledgements

We would like to thank Prof. M.E. Smith (Department of Physics, University of Warwick) for providing the NMR results. SJ thanks the Royal Thai Government and PSG thanks The Royal Society, UK for financial support.

References

1. Chraska, P., Dubsky, J., Kolman, B., Ilavsky, J. and Forman, J., Study of phase changes in plasma sprayed deposits. *J. Thermal. Spray. Technol*., 1992, **1**(4), 301–306.
2. Karunaratne, B. S. B. and Lewis, M. H., Plasma-sprayed ceramic coatings for SiAlON ceramics. *J. Eur. Ceram. Soc*., 1996, **16**, 1133–1139.
3. Chraska, P., Dubsky, J., Neufuss, K. and Pisacka, J., Alumina-base plasma-sprayed materials-Part 1: phase stability of alumina and alumina-chromia. *J. Thermal. Spray. Technol*., 1997, **6**(3), 320–326.
4. Ault, N. N., Characteristics of refractory oxide coatings produced by flame-spraying. *J. Am. Ceram. Soc*., 1957, **40**(3), 69–74.
5. Haffadine, J. P. and Thomas, A. G., Flame spraying as a method of fabrication dense bodies of alumina. *Powder Met*., 1964, **7**(14), 290–299.
6. McPherson, R., Formation of metastable phases in flame and plasma prepared alumina. *J. Mater. Sci*., 1973, **8**, 851–858.
7. McPherson, R., On the formation of thermally sprayed alumina coatings. *J. Mater. Sci*., 1980, **15**, 3141–3149.
8. Damani, R. J. and Makroczy, P., Heat treatment induced phase and microstructural development in bulk plasma sprayed alumina. *J. Eur. Ceram. Soc*., 2000, **20**, 867–888.
9. Niihara, K., New design concept of structural ceramic nanocomposites. *J. Ceram. Jpn*, 1991, **99**, 974–982.
10. Zhao, J., Stearns, L. C., Harmer, M. P., Chan, H. M., Miler, G. A. and Cook, R. F., Mechanical behavior of alumina-silicon carbide nanocomposites. *J. Am. Ceram. Soc*., 1993, **76**, 503–510.
11. Davidge, R. W., Brook, R. J., Cambier, F., Poorteman, M., Leriche, A., O'Sullivan, D., Hampshire, S. and Kennedy, T., Fabrication, properties and modelling of engineering ceramics reinforced with nanoparticles of silicon carbide. *Br. Ceram. Trans*., 1997, **96**(3), 121–127.
12. Kara, H. and Roberts, S. G., Polishing behaviour and surface quality of alumina and alumina/silicon carbide nanocomposites. *J. Am. Ceram. Soc*., 2000, **83**, 1219–1225.
13. Davidge, R. W., Twigg, P. C. and Riley, F. L., Effects of silicon carbide nano-phase on the wet erosive wear of polycrystalline alumina. *J. Eur. Ceram. Soc*., 1996, **16**, 799–802.
14. Sternitzke, M., Dupas, E., Twigg, P. and Derby, B., Surface mechanical properties of alumina matrix nanocomposites. *Acta. Mater*., 1997, **45**(10), 3963–3973.
15. Lawrence, C. W., Roberts, S. G., Derby, B. Microstructural requirements for alumina-SiC nanocomposites. In *Engineering with Ceramics*, ed. W.E. Lee and B. Derby. British Ceramic Proceedings, 1998, pp. 127–132.
16. Kara, H. *Polishing and Erosive Wear of Pressureless Sintered Low-SiC Alumina/SiC Nanocomposites*. DPhil Thesis, Oxford University, 2000.
17. Meinhold, R. H., Slade, R. C. T. and Newman, R. H., High Field MAS NMR, with simulations of the effects of disorder on lineshape, applied to thermal transformations of alumina hydrates. *Appl. Magn. Reson*., 1993, **4**, 121–140.
18. Slade, R. C. T., Southern, J. C. and Thompson, I. M., ^{27}Al Nuclear Magnetic Resonance Spectroscopy investigation of thermal transformation sequence of alumina hydrates, Part 2.—Boehmite, γ-AlOOH. *J. Mater. Chem*., 1991, **1**(5), 875–879.
19. Varma, H. K., Mani, T. V., Damodaran, A. D. and Warrier, K. G., K Characteristics of alumina powders prepared by spray-drying of boehmite Sol. *J. Am. Ceram. Soc*., 1994, **77**(6), 1597–1600.
20. Ananthakumar, S., Hareesh, U. S., Damodaran, A. D. and Warrier, K. G. K., Microwave processing of boehmite coated SiC composite precursors for alumina-silicon carbide nanocomposites. *J. Mater. Sci. Lett*., 1998, **17**, 145–148.
21. Borsa, C.E. *Fabrication and Mechanical Properties of Al_2O_3/SiC Nanocomposites*. DPhil Thesis, Oxford University, 1995.
22. Pawlowski, L., *The Science and Engineering of Thermal Spray Coatings*. John Wiley & Sons, 1995.